PCCP

ROYAL SOCIETY OF CHEMISTRY

PAPER

View Article Online
View Journal | View Issue

Cite this: *Phys. Chem. Chem. Phys.*, 2022, **24**, 17028

Oxygen deficiency in Sr_2FeO_{4-x}: electrochemical control and impact on magnetic properties†

Peter Adler, *[a] Liane Schröder,[a] Klaus Teske,[a] Manfred Reehuis,[b] Andreas Hoser,[b] Patrick Merz,[a] Walter Schnelle,[a] Claudia Felser[a] and Martin Jansen *[ac]

Received 11th May 2022,
Accepted 29th June 2022

DOI: 10.1039/d2cp02156k

rsc.li/pccp

The oxygen-deficient system Sr_2FeO_{4-x} was explored by heating the stoichiometric Fe^{4+} oxide Sr_2FeO_4 in well-defined oxygen partial pressures which were controlled electrochemically by solid-state electrolyte coulometry. Samples with x up to about 0.2 were obtained by this route. X-ray diffraction analysis reveals that the K_2NiF_4-type crystal structure (space group $I4/mmm$) of the parent compound is retained. The lattice parameter a slightly decreases while the c-parameter increases with increasing x, which is in contrast to the Ruddlesden–Popper system $Sr_3Fe_2O_{7-x}$ and suggests removal of oxygen atoms from FeO_2 lattice planes. The magnetic properties were studied by magnetization, ^{57}Fe Mössbauer, and powder neutron diffraction experiments. The results suggest that extraction of oxygen atoms from the lattice progressively changes the elliptical spiral spin ordering of the parent compound to an inhomogeneous magnetic state with coexistence of long-range ordered regions adopting a circular spin spiral and smaller magnetic clusters.

1. Introduction

Perovskite-related ferrates with iron in the high oxidation state +4 constitute an interesting class of transition metal (TM) oxides due to their peculiar electronic, magnetic, and structural properties. Formally, the electronic structure of Fe^{4+} oxides can be discussed starting from the $t_{2g}^3e_g^1$ ($S = 2$) ligand field configuration of $3d^4$ ions, where the high oxidation state of the TM ion gives rise to strong covalency of Fe–O bonding and in turn to strong hybridization between Fe 3d and O 2p orbitals. In the framework of configuration interaction models the iron(IV) oxides, along with Cu^{3+} and Ni^{3+} oxides,[1–4] belong to the class of negative-charge-transfer energy (negative-Δ) compounds, where the electronic ground state is rather dominated by holes in the oxygen bands (L^{-n}, n = 1, 2), *i.e.* by a d^5L^{-1} electron configuration instead of an ionic d^4 configuration.[5] Remarkable properties which are related to the negative-Δ situation are the metallic behavior of $SrFeO_3$,[6] a charge-disproportionation (CD) process which may be written as $2d^5L^{-1} \rightarrow d^5 + d^5L^{-2}$ or $2t_{2g}^3e_g^1 \rightarrow t_{2g}^3e_g^2 + t_{2g}^3$ in $CaFeO_3$,[7,8] $Sr_3Fe_2O_7$,[7,9–12] $CaCu_3Fe_4O_{12}$,[13] and Ca_2FeMnO_6,[14] pressure-induced insulator-to-metal and/or high-spin to low-spin transitions in $CaFeO_3$,[15] $Sr_3Fe_2O_7$,[16] and $CaCu_3Fe_4O_{12}$,[17] as well as antiferromagnetic ordering with different types of helical spin structures in $SrFeO_3$,[18] $CaFeO_3$,[8] cubic $BaFeO_3$,[19] and $Sr_3Fe_2O_7$.[20] In particular, $SrFeO_3$ features a sensitive response of the helical spin structure to temperature and magnetic fields,[21,22] which makes this system an interesting model case for topological spin textures in the absence of Dzyaloshinskii–Moriya interactions.[23]

Convenient ways for tuning the electronic and magnetic properties of TM oxides are cationic substitutions or variation of the oxygen content. In case of perovskite-related ferrates the great flexibility of the perovskite structure has allowed to vary the oxygen content in a wide range and thus to realize Fe in oxidation states between +2 and +4. For the $SrFeO_{3-x}$ system several structurally and magnetically distinct phases have been described,[24,25] namely metallic and helimagnetic $SrFeO_3$, $Sr_8Fe_8O_{23}$ ($SrFeO_{2.875}$) which reveals a charge-ordering transition,[26,27] partially frustrated $Sr_4Fe_4O_{12}$ ($SrFeO_{2.75}$) where only the Fe^{3+} fraction orders magnetically, the antiferromagnetic Brownmillerite $Sr_2Fe_2O_5$, and finally the Fe^{2+} oxide $SrFeO_2$ with infinite FeO_2 layers in the crystal structure.[28] Similarly, in the bilayer Ruddlesden-Popper system $Sr_3Fe_2O_{7-x}$ the iron oxidation state could be tuned between +4 and +2, but in contrast to the $SrFeO_{3-x}$ system no well-defined vacancy-ordered phases were found.[29] The end members of the former homogeneity range are $Sr_3Fe_2O_7$ (Fe^{4+})[30,31] and $Sr_3Fe_2O_5$ (Fe^{2+}).[32] As changes in the oxygen content lead to changes in the oxidation states and coordination of the iron ions, also the magnetic properties are substantially affected. Oxygen-deficient perovskite-related ferrates are not only of interest as potential magnetic materials

[a] *Max-Planck-Institut für Chemische Physik fester Stoffe, 01187 Dresden, Germany. E-mail: adler@cpfs.mpg.de*
[b] *Helmholtz-Zentrum für Materialien und Energie, 14109 Berlin, Germany*
[c] *Max-Planck-Institut für Festkörperforschung, 70569 Stuttgart, Germany. E-mail: m.jansen@fkf.mpg.de*

† Electronic supplementary information (ESI) available. See DOI: https://doi.org/10.1039/d2cp02156k

but also as mixed anionic conductors for applications in solid oxide fuel cells[33] and in oxygen-separating membranes[34] or as oxygen sources for NO oxidation.[35]

A less studied Fe^{4+} oxide is the K_2NiF_4-type phase Sr_2FeO_4 which was first reported by Scholder *et al.*[36] and has an insulating ground state, but in contrast to $Sr_3Fe_2O_7$ does not feature a CD of Fe^{4+}.[9,37] An unexpected oxygen-related phonon band in Raman spectra of Sr_2FeO_4 may indicate that the insulating ground state is associated with a tiny structural distortion which, however, has remained elusive so far.[38] Recently, we have shown that Sr_2FeO_4 adopts an elliptical spiral spin structure which shows a spin-flop-type reorientation in external magnetic field of about 5 T.[39] Sr_2FeO_4 can be considered as a negative-Δ insulator, which is supported by its high-pressure properties showing the disappearance of the additional Raman band near 6 GPa[38] and a concomitant change from a spiral to a ferromagnetic spin structure.[39,40] An insulator-to-metal transition near 18 GPa was attributed to the closure of the p–p-type excitation gap.[40] Only few substituted phases based on Sr_2FeO_4 were reported so far,[41–43] and to the best of our knowledge oxygen deficiency in the Sr_2FeO_{4-x} system has not been studied in detail. However, similar as for the 113 and 327 systems also for 214 a layered compound with Fe^{2+} in square planar coordination, Sr_2FeO_3, was synthesized.[44]

In the present study we have explored the oxygen-deficient system Sr_2FeO_{4-x} by heating fully oxidized Sr_2FeO_4 at increasing temperatures and a well-defined oxygen partial pressure. The oxygen contents were controlled and analyzed electrochemically using solid-state electrolyte coulometry. Sr_2FeO_{4-x} samples with oxygen deficiencies $0 < x \leq 0.2$ could be prepared by this route. Attempts to increase the oxygen deficiency further required heating at temperatures above 700 °C where decomposition into $Sr_3Fe_2O_{7-x}$ and SrO occurs. The impact of oxygen deficiency on the magnetic properties in Sr_2FeO_{4-x} was studied by magnetization, ^{57}Fe Mössbauer spectroscopy, and powder neutron diffraction experiments.

2. Experimental details

2.1. Synthesis of Sr_2FeO_4

Sr_2FeO_4 was prepared by solid state reaction of home-made SrO and Fe_2O_3 while applying elevated oxygen pressure. For the synthesis of SrO, 50 g $SrCO_3$ (Sigma-Aldrich, >99.99% metal basis) was mixed with 100 ml of H_2O, and HNO_3 (65% strength) was added with stirring until no gas evolution was evident. The solution was evaporated and the resulting $Sr(NO_3)_2$ was decomposed to SrO at 550 °C in dynamic vacuum in a Schlenk line. The purity of the product was verified by powder X-ray diffraction. For storage, the SrO was sealed in glass ampoules. Fe_2O_3 was synthesized by decomposition of $FeC_2O_4{\cdot}2H_2O$ (Alfa Aesar, Puratronic, 99.999% metal basis) in a tube furnace under a slow flow of oxygen at 350 °C and prior to use stored in an argon-filled glove box.

A mixture of SrO and Fe_2O_3 with a slight excess of SrO (molar ratio of 4.02/1.00) was finely ground in an agate mortar in a glove box under argon atmosphere. The mixture was placed in a corundum finger crucible, covered with a thin layer of SrO and a gold lid on top. High oxygen pressure synthesis was performed in a specifically designed, scale-resistant steel autoclave described earlier.[45] The charged crucible was placed in the autoclave, which was closed, loaded with 10 ml of liquid O_2 and subsequently heated at a rate of 20 K h^{-1} to 773 K, which generates an O_2 pressure of 2.5 kbar (free volume ~15 ml). This temperature was kept for 72 hours, next the heating source was switched off and the autoclave was allowed to cool to room temperature with a rate of about 300 K h^{-1}. The reaction product as obtained was reground, and annealed along the same procedure as described, once again. Samples with enrichment of the isotope ^{57}Fe to 10 or 20% for high-pressure synchrotron Mössbauer studies[39] were obtained by using isotopically enriched Fe_2O_3 as starting material.

2.2. Characterization methods

Powder X-ray diffraction (PXRD) was performed using a Huber G670 camera (Guinier technique, Co $K\alpha_1$ radiation, λ = 1.788965 Å, diffraction range $10^\circ \leq 2\theta \leq 100^\circ$ in steps of 0.005°). Rietveld refinement[46] of the PXRD data of Sr_2FeO_4 was performed with the program WinCSD.[47]

Thermogravimetric (TGA) analysis of Sr_2FeO_4 was carried out on a Netzsch STA 449 F3 thermoanalyzer. About 30 mg of the sample was placed in a corundum crucible, which was heated at a rate of 5 K min^{-1} in the range of 300–1073 K under dynamic argon flow. The sample was kept at 1073 K (800 °C) for 4 hours where no further weight loss was observed. Finally, the sample was cooled down again.

Magnetization measurements of Sr_2FeO_{4-x} were recorded on samples sealed in Suprasil quartz tubes under He using an MPMS3 (Quantum Design) magnetometer in the temperature range of 1.8 to 400 K, in zero-field cooling (zfc) and field-cooling (fc) modes in applied fields up to 7 T. Isothermic magnetization measurements were performed after zero-field cooling by field ramping between 0 and 7 T.

^{57}Fe Mössbauer spectra were collected at various temperatures using a standard WissEl spectrometer operated in the constant acceleration mode (^{57}Co/Rh source) and a Janis SHI 850-5 closed cycle refrigerator. Powder samples of Sr_2FeO_{4-x} containing about 10 mg Fe cm^{-2} were homogeneously distributed in an acrylic glass sample container with an inner diameter of 13 mm. In some cases the samples were diluted with BN to ensure homogeneous distribution. All isomer shifts are given relative to α-iron. The data were evaluated with the MossWinn program[48] using the thin absorber approximation. To model the shape of the spectra in the magnetically ordered phases hyperfine field distributions were either derived by the Hesse–Rübartsch method implemented in MossWinn or Gaussian hyperfine field distributions were assumed.

Magnetic structures were analyzed by powder neutron diffraction (PND) on two Sr_2FeO_{4-x} samples with x = 0.133(3) and x = 0.158(6). About 3 grams of material were placed in a vanadium sample container. Data were collected using the diffractometer E2 at the BER II reactor of the Helmholtz-Zentrum

Berlin. This instrument is equipped with a pyrolytic graphite (PG) monochromator selecting the neutron wavelength λ = 2.380 Å. PND patterns were recorded at 1.8 and 80 K, well below and above the magnetic ordering temperatures, respectively. Additional PND patterns were measured within this temperature range to determine the temperature dependence of the lattice parameters and of the magnetic order parameters. The powder patterns were collected in the range of diffraction angles from 3.7° to 79.4°. Rietveld refinements of the PND data were carried out with the program *FullProf*,[49] using the nuclear scattering lengths b(O) = 5.805 fm, b(Fe) = 9.54 fm, and b(Sr) = 7.02 fm.[50] The magnetic form factors of the Fe atoms were taken from ref. 51.

2.3. Solid-state electrolyte coulometry

Solid-state electrolyte coulometry (SEC) was employed to analyze and adjust the oxygen content of Sr_2FeO_{4-x}, and to establish the corresponding p_{O_2}-T-x-diagram. The basic principle of the technique and an overview on its applications has been detailed in ref. 52–54. The setup used for the studies presented here is sketched in Fig. 1. The system operates in a carrier gas mode and consists of two identical solid-state electrolyte (SE) SGM5EL ZIROX cells (doped zirconium oxide, ZIROX-Sensoren und Elektronik GmbH, 17489 Greifswald). Each cell has two electrode systems for potentiometric measurement of the chemical potential of oxygen and coulometric dosing or pumping of oxygen, respectively. The cells are positioned upstream (cell 1) and downstream (cell 2) of a quartz-tube reactor containing the sample whose change in oxygen content in course of the solid-gas interaction is to be studied as a function of temperature. In this setup the space containing the specimen to be equilibrated is thermally decoupled from the SE cells, thus the latter may operate constantly at such a temperature which is optimal for the solid electrolyte (~750 °C for doped zirconium oxide). This measure taken admits to conveniently optimize the parameters of the gas-solid interaction (temperature program, geometry and material of the reactor) appropriate to the sample under investigation.[55] Current I, voltage U, O_2 concentration, and temperature of each SE cell, as well as the temperature of the sample were recorded using a customized computer program based on LabVIEW.

As carrier gases Ar, or gas mixtures Ar–H_2 and Ar–H_2–H_2O, respectively, were used. The range of partial pressures of oxygen realizable in Ar/O_2 is 10^{-6} to 10^{-3} bar and for Ar–H_2–H_2O mixtures 10^{-32} to 10^{-9} bar. For the latter, the oxygen partial pressures evolving as function of temperature for selected H_2/H_2O ratios are documented in Fig. S1 and Table S1 (ESI†).

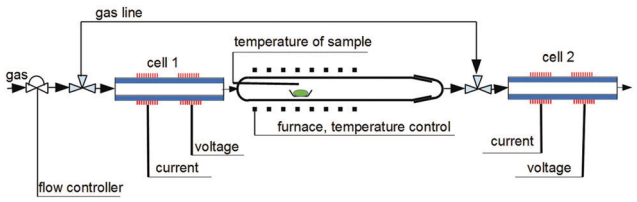

Fig. 1 Solid state electrolyte coulometry. Sketch of the experimental set up.

The actual oxygen chemical potential in the carrier gas was controlled in the upstream cell, whereas the uptake or loss of oxygen of the sample during the gas–solid equilibration was monitored in the downstream cell.

The mass of oxygen exchanged during solid-gas equilibration, Δm_{O_2}, is obtained from Faraday's law,

$$\Delta m_{O_2} = \frac{M_{O_2}}{F \times z} \times \int_{t=\text{start}}^{t=\text{end}} (I_0 - I_t)\mathrm{d}t \quad (1)$$

where I_0 is the constant basic oxygen dosing current, I_t is the current registered in the downstream cell at time t, M_{O_2} is the molecular mass of oxygen, F the Faraday constant, and z = 4 the number of electrons transferred. The change Δx in oxygen stoichiometry for a sample with mass m and molecular weight M_s is obtained as

$$\Delta x = \Delta m_{O_2} \times M_s/(m - \Delta m_{O_2})M_{O_2}. \quad (2)$$

The actual stoichiometry of the reduced specimen can be derived if the gas-solid reaction starts from a material with a well-defined oxygen content or if it leads to a well-defined final product. The samples of Sr_2FeO_4 used as starting materials were saturated with respect to oxygen content by annealing under elevated oxygen pressure.

The present experiments were carried out under the following conditions: depending on the size of the sample, the reaction chamber (quartz tube) had a diameter of approx. 18 mm outside and 16 mm inside, or alternatively 25/23 mm. A section of ~17 cm of the total length of the reaction chamber (22 cm) was heated by a tube furnace. The sample was located in a quartz boat in the middle of the furnace. A thermocouple was attached close to the reaction site in a ''quartz nose'', in order to enable a correct and continuous temperature registration at the reaction location.

In an exemplary run, an Ar gas flow of 5 l h^{-1} with about 3×10^{-6} bar O_2 is used as carrier gas, the Sr_2FeO_4 samples are heated at a rate of 7 °C min^{-1} and held at the targeted temperatures for 8 h. The O_2 activity is fine-tuned *via* the dosing current I_0 (~10 mA) of the upstream cell.

3. Results and discussion

3.1. Synthesis and characterization of Sr_2FeO_4

The synthesis of Sr_2FeO_4 is challenging because of the fact that the compound decomposes above 700 °C into the Ruddlesden-Popper phase $Sr_3Fe_2O_{7-x}$ and SrO. In previous work Sr_2FeO_4 was prepared either by heating of $SrCO_3$ and Fe_2O_3 at 1300 °C and subsequent conversion of the two-phase primary product $Sr_3Fe_2O_{7-x}$/SrO to Sr_2FeO_4 in a flow of high-pressure oxygen (200 bar) at 750 °C,[56] or by direct reaction from SrO and Fe_2O_3 at 650 °C in flowing O_2 atmosphere at ambient pressure.[37] The latter samples always contained a certain amount of unreacted Fe_2O_3. Here, we have successfully prepared phase-pure Sr_2FeO_4 by reaction of SrO and Fe_2O_3 in an autoclave at an oxygen pressure of 2500 bar at a moderate temperature of 500 °C. A Rietveld profile analysis (Fig. 2(a)) underlines the absence of any impurity phase,

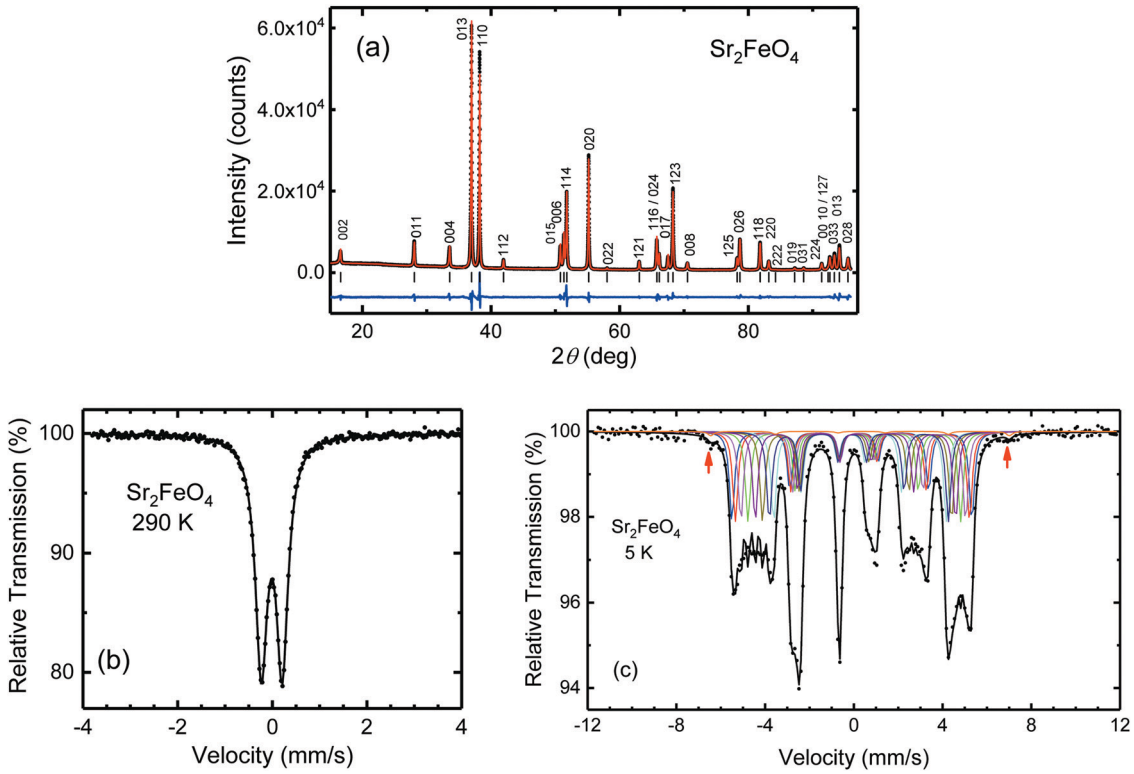

Fig. 2 Characterization of Sr_2FeO_4 obtained by high-pressure synthesis. (a) Rietveld analysis of the powder X-ray diffraction pattern. Dots correspond to the experimental data, red solid lines to the calculated pattern, blue solid lines to the difference pattern, and the tick bars to the peak positions. (b) Mössbauer spectrum at 290 K. The spectrum was fitted with a single quadrupole doublet with isomer shift IS = −0.014(1) mm s^{-1} and quadrupole splitting QS = 0.444(1) mm s^{-1} confirming the Fe^{4+} oxidation state. (c) Mössbauer spectrum at 5 K. The red arrows indicate a tiny Fe^{3+} fraction of ∼1% with B_{hf} ∼ 42 T which is seen in addition to the complex Fe^{4+} hyperfine pattern here approximated by 8 sextets.

and has resulted in crystal structure data (*cf.* Table S2, ESI†) fully complying with those from previous studies.[56] Thermogravimetic analysis of a sample of Sr_2FeO_4 at 800 °C in an argon flow resulted in the composition $Sr_2FeO_{4.00(2)}$ if decomposition of the sample to stoichiometric $Sr_3Fe_2O_6$ and SrO is assumed.

Any oxygen deficiency in Sr_2FeO_4 can also be estimated using ^{57}Fe Mössbauer spectra. At room temperature (see Fig. 2(b)) the spectrum consists of a simple quadrupole doublet, assuring the absence of any Fe_2O_3 impurity and confirming that virtually all iron ions exist in the +4-oxidation state. Even more sensitive to small Fe^{3+} components is the Mössbauer spectrum in the magnetically ordered phase at 5 K which is shown Fig. 2(c). The spectrum is characterized by a complex hyperfine field (B_{hf}) distribution which reflects the elliptical spiral spin structure of Sr_2FeO_4 and was approximated by a superposition of eight hyperfine sextets having a typical Fe^{4+} isomer shift IS = 0.07 mm s^{-1}.[39] Detailed inspection of the spectrum reveals a tiny additional hyperfine component with an enlarged B_{hf} of ∼42 T and an intensity contribution of about 1% (marked by arrows in Fig. 2(c)) which is attributed to Fe^{3+}. In different preparation runs the intensity fraction of this component slightly varied but was always ≤2%. Thus, using the Mössbauer spectra we estimate the oxygen deficiency in the high-pressure synthesized samples as ≤0.01. The good agreement with the results from the TGA reduction experiment at 800 °C in argon atmosphere indicates that under these conditions indeed reduction to the stoichiometric Fe^{3+} phase $Sr_3Fe_2O_6$ was achieved.

3.2. Investigation of the oxygen homogeneity range in Sr_2FeO_{4-x} by SEC

In exploring the homogeneity range of Sr_2FeO_{4-x}, pristine samples of Sr_2FeO_4 were equilibrated at constant temperatures and in argon carrier gas flows of defined oxygen partial pressure. The release of oxygen during solid/gas equilibration of the sample was compensated and monitored in the downstream cell, see section Experimental details.

A representative plot of the reduction process as function of time for target temperatures up to 500 °C is displayed in Fig. 3(a). Here, and in all other respective experiments two steps of reduction are apparent. The desorption of oxygen starts at about 150 °C with the maximum occurring at 300 °C. A second peak is apparent for temperatures ≥400 °C and represents further oxygen desorption in the Sr_2FeO_{4-x} phase. Integration of the temperature programmed oxygen desorption (TPOD) reaction curves yields the change in oxygen content Δ*x* according to eqn (1) and (2) (Fig. 4(a)). Since during temperature rise the sample and gas phase are not always in equilibrium, details of the shape of the TPOD curve depend on the experimental conditions applied, as sample mass, gas flow and temperature gradient. Using this method oxygen-deficiency in Sr_2FeO_{4-x}

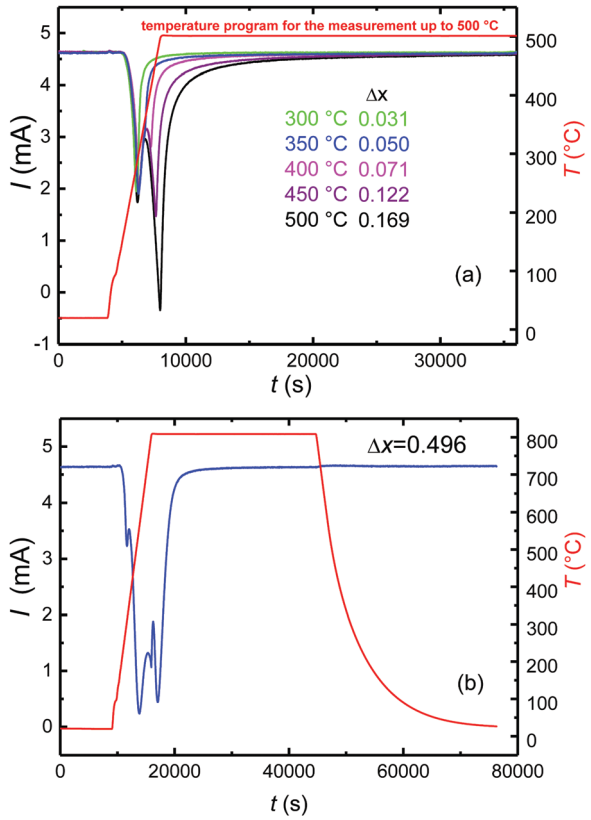

Fig. 3 Temperature programmed desorption curves for Sr_2FeO_{4-x} obtained by heating to the indicated temperatures. (a) Final temperature 300 to 500 °C, (b) final temperature 808 °C. The titration current I is represented as a function of time t. The temperature profiles for heating to 500 °C and to 808 °C are also shown. Typical sample masses were about 100 mg and the oxygen partial pressure was 3×10^{-6} bar.

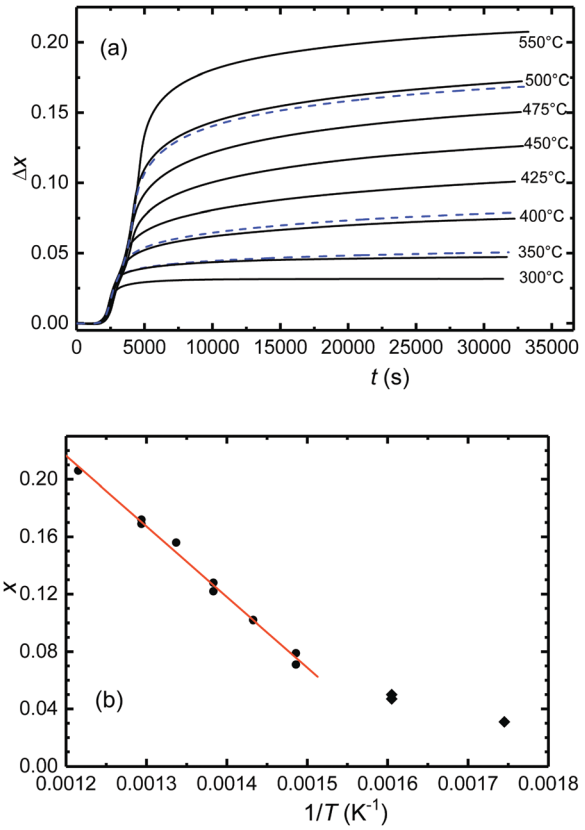

Fig. 4 (a) Change of oxygen deficiency x in Sr_2FeO_{4-x} during the reaction in argon ($p_{O_2} = 3 \times 10^{-6}$ bar) with different final temperatures. If the initial phase is assumed to be stoichiometric Sr_2FeO_4, then $\Delta x = x$. (b) Oxygen deficiency as a function of inverse temperature. A linear relation is found between 400 °C (673 K) and 550 °C (823 K). The dashed blue lines correspond to a second independent experiment at the respective temperature.

with x up to about $\sim$0.20 was realized, which corresponds to Fe^{3+} fractions up to about 40%. Between 400 and 550 °C (673 and 823 K) a linear relation between x and inverse temperature was observed (Fig. 4(b)).

Running the experiments at even higher temperatures of up to 800 °C leads to further reduction steps (Fig. 3(b)) which according to PXRD characterization (see Fig. 5) is accompanied by decomposition of Sr_2FeO_{4-x} finally leading to the formation of $Sr_3Fe_2O_6$ according to

$$2Sr_2FeO_4 \rightarrow Sr_3Fe_2O_6 + SrO + \tfrac{1}{2}O_2.$$

At the same time this decomposition reaction demarcates the limit of oxygen deficiency in Sr_2FeO_{4-x} which can be achieved with this method. The change $\Delta x = 0.496$ in oxygen content obtained by reduction at 800 °C suggests a full reduction of Fe^{4+} in stoichiometric Sr_2FeO_4 to Fe^{3+} in $Sr_3Fe_2O_6$ which compares well with the TGA result.

Samples of Sr_2FeO_{4-x} with different values of x were synthesized by choosing different target temperatures and subsequent cooling. The samples were characterized by PXRD, a representative set of patterns is displayed in Fig. 5. Up to $x \sim 0.2$ (heating up to 550 °C) the patterns still exhibit only reflections which are typical for the tetragonal K_2NiF_4-type crystal structure (space group $I4/mmm$) adopted by stoichiometric Sr_2FeO_4. Line broadening which increases with x may reflect strain effects owing to the oxygen desorption process, stacking faults,[39] and a certain inhomogeneity in x. For a sample with even higher $x = 0.22$ obtained by annealing at 600 °C a broad pattern was observed (not shown), which still shows the main reflections of the K_2NiF_4-type structure but also additional broad peaks. Further increase of temperature leads to degradation into $Sr_3Fe_2O_{7-x}$ (space group $I4/mmm$) and SrO. These results suggest that Sr_2FeO_{4-x} samples with x up to $\sim$0.2 can be prepared by the present route, but decomposition occurs for larger x requiring higher reaction temperatures. In Fig. 6 the lattice parameters a and c as well as the cell volume V are shown for all samples prepared within this study and where the parent structure was retained. It is evident that the c parameter and V increase with increasing x whereas a slightly decreases. The variation of a with x in the Sr_2FeO_{4-x} system is in sharp contrast to the behavior of a in the $Sr_3Fe_2O_{7-x}$ system,[31] which contains double layers of FeO_m polyhedra (m = 5, 6) and is the n = 2 member of the $Sr_{n+1}Fe_nO_{3n+1}$ Ruddlesden-Popper series. For $Sr_3Fe_2O_{7-x}$ the lattice parameter a increases linearly with

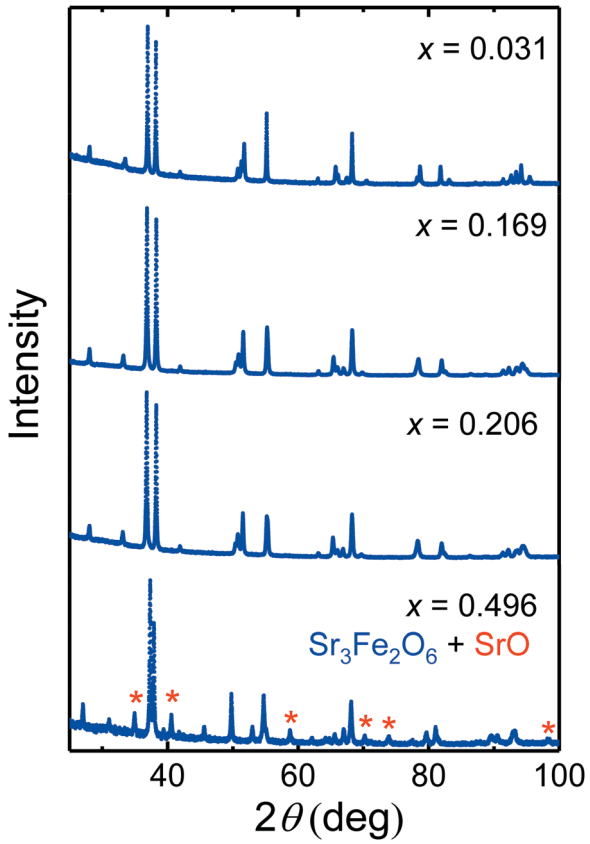

Fig. 5 Powder X-ray diffraction patterns of nominal Sr_2FeO_{4-x} samples with increasing oxygen deficiency x. The analysis of the PND pattern of the sample with x = 0.496 revealed complete decomposition to $Sr_3Fe_2O_6$ and SrO, where the peaks corresponding to SrO are marked by an asterisk.

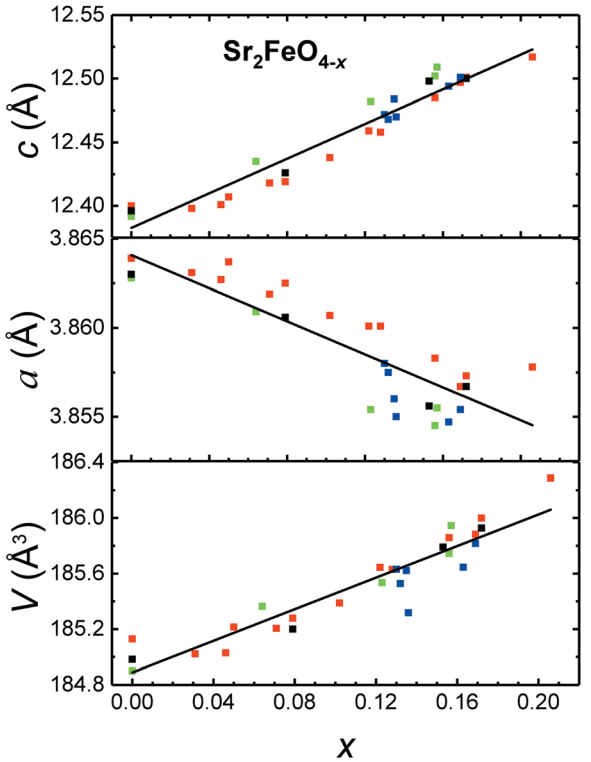

Fig. 6 Lattice parameters and volume per formula unit for Sr_2FeO_{4-x} as function of x as determined from XRD patterns at room temperature. The different colors correspond to different sample preparation series. The solid lines are linear fits to all data sets.

increasing x, *i.e.* with increasing Fe^{3+} fraction, whereas the lattice parameter c shows a non-monotonic variation. This can be related to the fact that in $Sr_3Fe_2O_{7-x}$ the oxygen defects are created in the c direction, namely the oxygen atoms which connect the FeO_6 octahedra of the double layers *via* corner-sharing in stoichiometric $Sr_3Fe_2O_7$ are removed. Finally, this leads to square pyramidal coordination of Fe^{3+} in $Sr_3Fe_2O_6$.[31] The different behavior of a in Sr_2FeO_{4-x} suggests that mainly O atoms are removed from the FeO_2 layers in the ab plane. Then two opposing trends occur: on the one hand, the smaller Fe^{4+} ions are replaced by larger Fe^{3+} ions which should lead to an increase in a but on the other hand, the removal of O atoms from the layers leads to a collapse in a such that the overall variation of a with x is quite small. The increase in c mainly reflects the larger size of Fe^{3+} ions compared to Fe^{4+} ions. These considerations are in agreement with the different hydride reduction mechanisms proposed for $Sr_3Fe_2O_7$ and Sr_2FeO_4.[32,44] While for the former the reduction to $Sr_3Fe_2O_5$ proceeds *via* $Sr_3Fe_2O_6$ as intermediate phase, the latter was suggested to be reduced directly to Sr_2FeO_3 without intermediate phases.[44]

3.3. Magnetic properties of Sr_2FeO_{4-x}

The peculiar electronic situation in strongly covalent Fe(IV) oxides, which is characterized by a negative charge-transfer energy,[5] frequently gives rise to antiferromagnetic ordering with helical spin structures. Recently it was demonstrated that Sr_2FeO_4 adopts an elliptical spin spiral mainly oriented in the ab plane which undergoes a spin-flop transition in external magnetic fields of about 5 T.[39] To study the impact of oxygen deficiency, the magnetic properties of Sr_2FeO_{4-x} samples with x = 0.13 and 0.16 were investigated by magnetization, powder neutron diffraction, and ^{57}Fe Mössbauer measurements.

Magnetization measurements. In Fig. 7 we compare the magnetic susceptibilities $\chi(T)$ and inverse susceptibilities $\chi^{-1}(T)$ of oxygen-deficient $Sr_2FeO_{3.87}$ with those of the parent compound Sr_2FeO_4. The $\chi(T)$ curves of Sr_2FeO_4 (Fig. 7(a)) exhibit a maximum near 60 K which is the signature of antiferromagnetic order. According to specific heat data the Néel temperature is 55.8 K.[39] The field dependence of the $\chi(T)$ data for temperatures below the maximum reflects the spin-flop transition in Sr_2FeO_4 which also gives rise to a non-linearity in the magnetization curves $M(H)$ (Fig. 8). A further weak cusp is seen in low-field zfc data of Sr_2FeO_4 while fc data only reveal an inflection. As the strength of this low-temperature feature varies in different samples and it shows some frequency dependence in ac susceptibility data[39] it is probably related to disorder effects owing to residual oxygen defects. A similar but now very pronounced cusp at 9 K is observed in the low-field zfc susceptibility data of $Sr_2FeO_{3.87}$ which is suppressed in larger magnetic fields (Fig. 7(b)). The irreversibility between zfc and fc data at low field suggests that

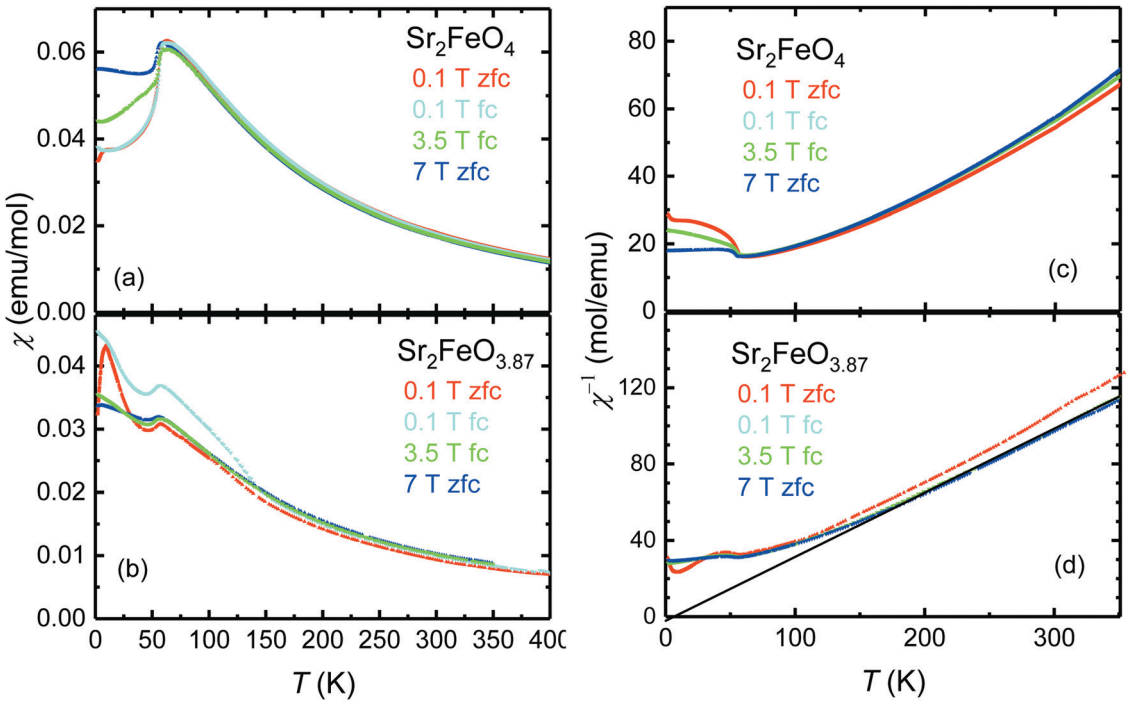

Fig. 7 Comparison of the magnetic susceptibilities χ [(a), (b)] and inverse susceptibilities χ^{-1} [(c), (d)] as a function of temperature of Sr_2FeO_4 and $Sr_2FeO_{3.87}$.

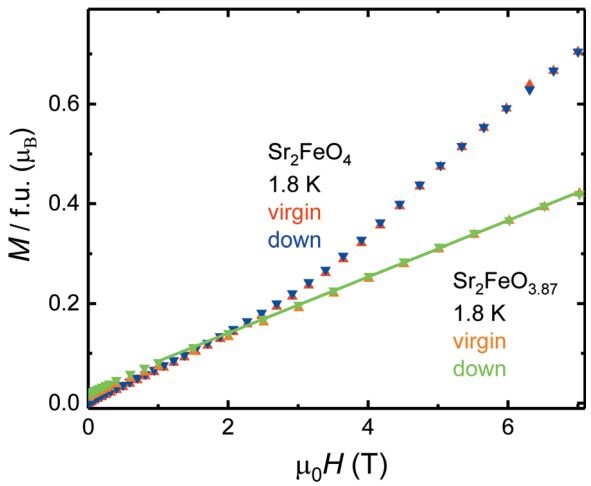

Fig. 8 Comparison of the field dependence of the magnetic moments $M(H)$ at T = 1.8 K of Sr_2FeO_4 and $Sr_2FeO_{3.87}$.

the magnetic order is perturbed by the oxygen vacancies and glassy components contribute to the magnetism. Nevertheless, a cusp near 57 K which occurs under zfc as well as fc protocol and is independent of the magnetic field, suggests that $Sr_2FeO_{3.87}$ still exhibits long-range antiferromagnetic ordering with a similar T_N as in Sr_2FeO_4. An additional feature near 150 K seen in the fc data of $Sr_2FeO_{3.87}$ at 0.1 T is probably not intrinsic to the main phase. In contrast to Sr_2FeO_4 the $\chi(T)$ data at low temperatures and higher fields are essentially independent of the field and in fact, the $M(H)$ curves of $Sr_2FeO_{3.87}$ at 1.8 K shown in Fig. 8 are linear between 1 and 7 T. These results suggest that the spin-flop transition of the parent compound is suppressed in the oxygen-deficient material. A non-linearity in $M(H)$ below 1 T and a small remanent magnetic moment indicate a tiny ferromagnetic signal. Similar results were obtained for a sample with slightly higher oxygen deficiency ($Sr_2FeO_{3.84}$, see Fig. S2, ESI†).

For $Sr_2FeO_{3.87}$ a Curie–Weiss (CW) analysis in the paramagnetic regime using the linear region in the $\chi^{-1}(T)$ data collected at 7 T (200–300 K) results in an effective magnetic moment μ_{eff} of 4.92 μ_B which is somewhat smaller than the spin-only value expected for a mixed-valence Fe^{4+}/Fe^{3+} system with Fe^{4+} moments of 4.9 μ_B and Fe^{3+} moments of 5.9 μ_B. The corresponding θ_{CW}-parameter of +7 K in the CW law [$\chi(T) = C/(T - \theta_{CW})$, C is the Curie constant] suggests the presence of competing exchange interactions, where compared to Sr_2FeO_4 the relative strength of ferromagnetic interactions is reduced with respect to antiferromagnetic interactions. In the $\chi^{-1}(T)$ data of Sr_2FeO_4 no well-defined linear region can be identified up to 350 K but the data indicate strong ferromagnetic correlations.

Mössbauer spectroscopy. To study the evolution of the magnetic structure with oxygen deficiency we have measured Mössbauer spectra of Sr_2FeO_{4-x} samples with different x. The spectra of the parent compound Sr_2FeO_4 at low temperatures exhibit a peculiar asymmetric shape,[9,37] which can be considered as the signature of the elliptical spiral spin structure giving rise to a characteristic distribution of hyperfine magnetic fields B_{hf} and an associated modulation of the quadrupole interaction parameter 2ε.[39] The latter depends on the orientation angle between B_{hf} and the principal axis V_{ZZ} of the electric field

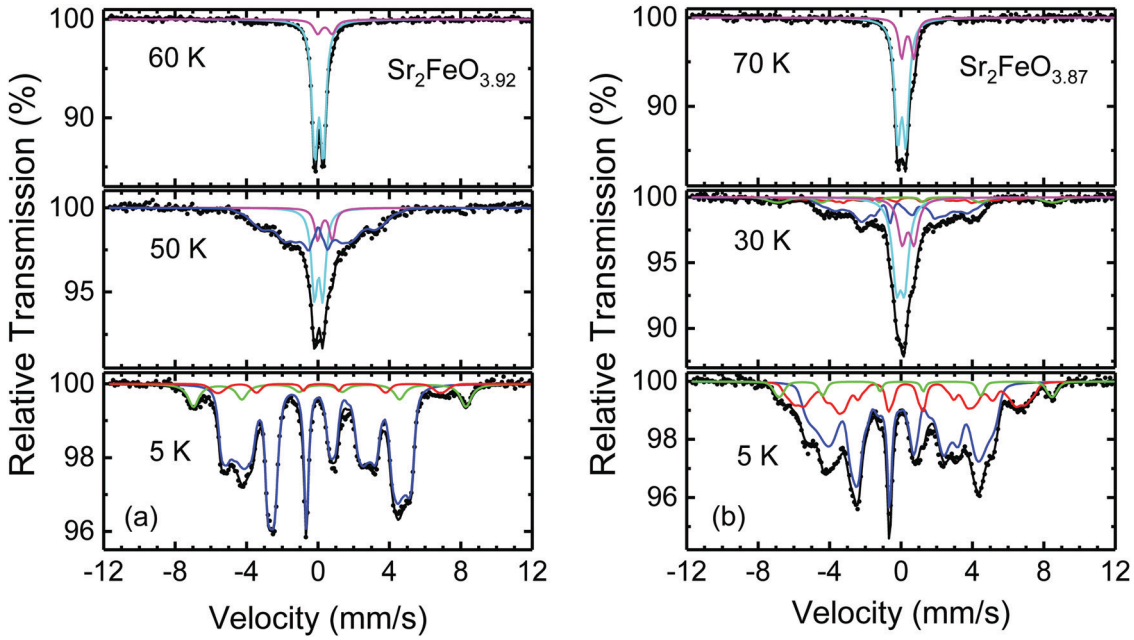

Fig. 9 Mössbauer spectra of oxygen-deficient $Sr_2FeO_{3.92}$ (a) and $Sr_2FeO_{3.87}$ samples (b) measured at the indicated temperatures. Dots correspond to the experimental data, solid lines to the best fits. The subspectra are shown as colored lines (blue and cyan correspond to magnetically ordered and paramagnetic Fe^{4+}, red and green to magnetically ordered Fe^{3+}, and pink to paramagnetic Fe^{3+} sites, respectively). The sample of $Sr_2FeO_{3.87}$ was part of the batch investigated by PND.

gradient tensor. The shape of the Mössbauer spectrum at 5 K of a sample with composition $Sr_2FeO_{3.92}$ shown in Fig. 9(a) is still reminiscent of that of the parent phase but additional components with enhanced hyperfine fields are apparent. The latter can be attributed to Fe^{3+} sites which are created owing to the oxygen deficiency. The essential shape of the spectrum could be reproduced with a Fe^{4+} component having an isomer shift IS = 0.08 mm s^{-1} and a B_{hf} distribution ($\langle B_{hf}\rangle$ = 28.5 T) which was obtained according to the Hesse-Rübartsch method and two Fe^{3+} components (IS = 0.40 mm s^{-1}) differing in their B_{hf} values ($\langle B_{hf}\rangle$ of 47.4 and 38.8 T, respectively). Similar as for Sr_2FeO_4, a linear correlation between B_{hf} and 2ε was assumed for the Fe^{4+} distribution. The extracted B_{hf} distribution (Fig. S3, ESI†) still reveals characteristic features of an elliptical spin spiral but the distribution is more complex which reflects modifications caused by the Fe^{3+} sites. Remarkably, the spectrum at 50 K reveals already about 30% of paramagnetic phase which indicates that in several domains of the $Sr_2FeO_{3.92}$ sample the magnetic ordering temperature is reduced. In the paramagnetic phase at 60 K the spectrum is well described by a superposition of two quadrupole doublets corresponding to Fe^{4+} and Fe^{3+}, respectively.

As expected, the Mössbauer spectra of a sample with composition $Sr_2FeO_{3.87}$ exhibit an enhanced fraction of Fe^{3+} sites (Fig. 9(b)). For fitting the complex shape of the spectrum at 5 K we extracted B_{hf} distributions for the Fe^{4+} component (IS = 0.07 mm s^{-1}, $\langle B_{hf}\rangle$ = 25 T) and for the broad major Fe^{3+} contribution ($\langle B_{hf}\rangle$ = 37 T) using the Hesse-Rübartsch method, while a smaller and less broad component with larger B_{hf} values ($\langle B_{hf}\rangle$ = 47.5 T) was described by a Gaussian B_{hf} distribution. For the Fe^{4+} component still a linear correlation between B_{hf} and 2ε was assumed, for the Fe^{3+} components a single 2ε and equal IS = 0.39 mm s^{-1} were used. The shape of the B_{hf} distribution of Fe^{4+} (Fig. S3, ESI†) differs from that of the parent phase which suggests that the spin structure is modified. The strong disturbance of the spin structure by the oxygen deficiency is also apparent from the presence of about 50% paramagnetic phase even at 30 K which is well below the T_N determined by neutron diffraction (see below). Similar spectra were obtained for a $Sr_2FeO_{3.84}$ sample but the fraction of magnetically ordered sites at 30 K is even smaller than in the $Sr_2FeO_{3.87}$ sample (see Fig. S4, ESI†).

The low-temperature spectra of all Sr_2FeO_{4-x} samples studied in this work revealed two different Fe^{3+} components, one with larger and one with smaller B_{hf} values. We have observed that samples from different reduction runs but with comparable oxygen deficiencies x resulted in different ratios of the two Fe^{3+} components. For instance, in the 5 K Mössbauer spectrum of a sample of $Sr_2FeO_{3.88}$ the area fraction of the Fe^{3+} component with larger B_{hf} (16%, Fig. S5, ESI†), is considerably enhanced compared to that (6%) in the spectrum of the $Sr_2FeO_{3.87}$ sample shown in Fig. 9(b). Remarkably, also the fraction of magnetically ordered sites at 30 K in the $Sr_2FeO_{3.88}$ sample is enhanced. The coexistence of magnetically ordered and collapsed phase below T_N suggests that the statistical extraction of oxygen atoms from Sr_2FeO_4 leads to fragmentation of the magnetic exchange network which results in magnetically ordered regions differing in size and ordering or freezing temperatures. It may be anticipated that removal of apical oxygen atoms has a less drastic effect for the magnetic exchange than the removal of oxygen atoms from the

FeO_2 layers. A different ratio between apical and layer oxygen defects could be the reason for the differences in the low-temperature Mössbauer spectra of samples from different reduction runs. If we assign the Fe^{3+} component with larger B_{hf} to Fe^{3+} sites from regions where an apical O atom has been removed, it appears reasonable that at a given temperature a larger fraction of magnetically ordered regions persists in samples where the large B_{hf}-component dominates. Then the Fe^{3+} signal with smaller B_{hf} corresponds to regions where O atoms were removed from the layers, and thus for samples where this type of Fe^{3+} sites dominate, the fraction of magnetically ordered sites at a given temperature is smaller. It cannot be readily decided whether the oxygen vacancies occur around Fe^{3+} or Fe^{4+} sites. In the oxygen deficient $SrFeO_{3-x}$ system the formation of square-pyramidal $Fe^{4+}O_5$ units is known,[24] whereas in the $Sr_3Fe_2O_{7-x}$ system $Fe^{3+}O_5$ units occur.[31] Our observations suggest that in different sample reduction runs somewhat different microstructures leading to differences in the local Fe^{3+} environment were produced. Unfortunately, attempts to control the microstructure by varying the reduction conditions were not conclusive.

Powder neutron diffraction studies. To clarify the influence of oxygen deficiency on the magnetic structure of Sr_2FeO_{4-x}, PND patterns of two samples with $x = 0.133(3)$ and $x = 0.158(6)$ were collected at 1.8 and 80 K, *i.e.* well in the magnetically ordered and in the paramagnetic state, respectively. For obtaining sufficient amount of material for the PND studies samples from different SEC reduction runs with comparable values of x were combined. In Fig. 10 the PND patterns of $Sr_2FeO_{3.87}$ and $Sr_2FeO_{3.84}$ are compared with those of the stoichiometric sample Sr_2FeO_4 which was investigated in our previous study.[39] The nuclear structures were refined in the tetragonal space group $I4/mmm$, and the results of the refinements are summarized in Table 1. Because of the limited range of diffraction angles 2θ, and the relatively large neutron wavelength of 2.380 Å it was not possible to determine the oxygen occupancies with good accuracy, but initial refinements of the oxygen occupancies indicated that oxygen atoms are mainly removed from the FeO_2 layers. Therefore, in the final refinements we have assumed full occupancy of the O1 atoms at the Wyckoff position 4e(0,0,z), while the occupancy of the O2 atoms at the Wyckoff position 4c(0,$\frac{1}{2}$,0) was fixed to the values calculated from the oxygen deficiency according to the SEC data. On the other hand, the structural parameters of Sr_2FeO_4, $Sr_2FeO_{3.87}$ and $Sr_2FeO_{3.84}$ could be reasonably well determined (see Table 1) although a certain deviation between calculated and observed lineshapes may indicate strain effects, lattice faults, and/or inhomogeneity in x, in agreement with the XRD study. The parameters of Sr_2FeO_4 obtained from neutron data at 80 K agree well with those from synchrotron data collected at 100 K.[39] A major goal of these refinements was to determine the overall scale factor with good accuracy which is needed to determine precisely the magnetic order parameters. In contrast to the refinement of the crystal structure it was possible to

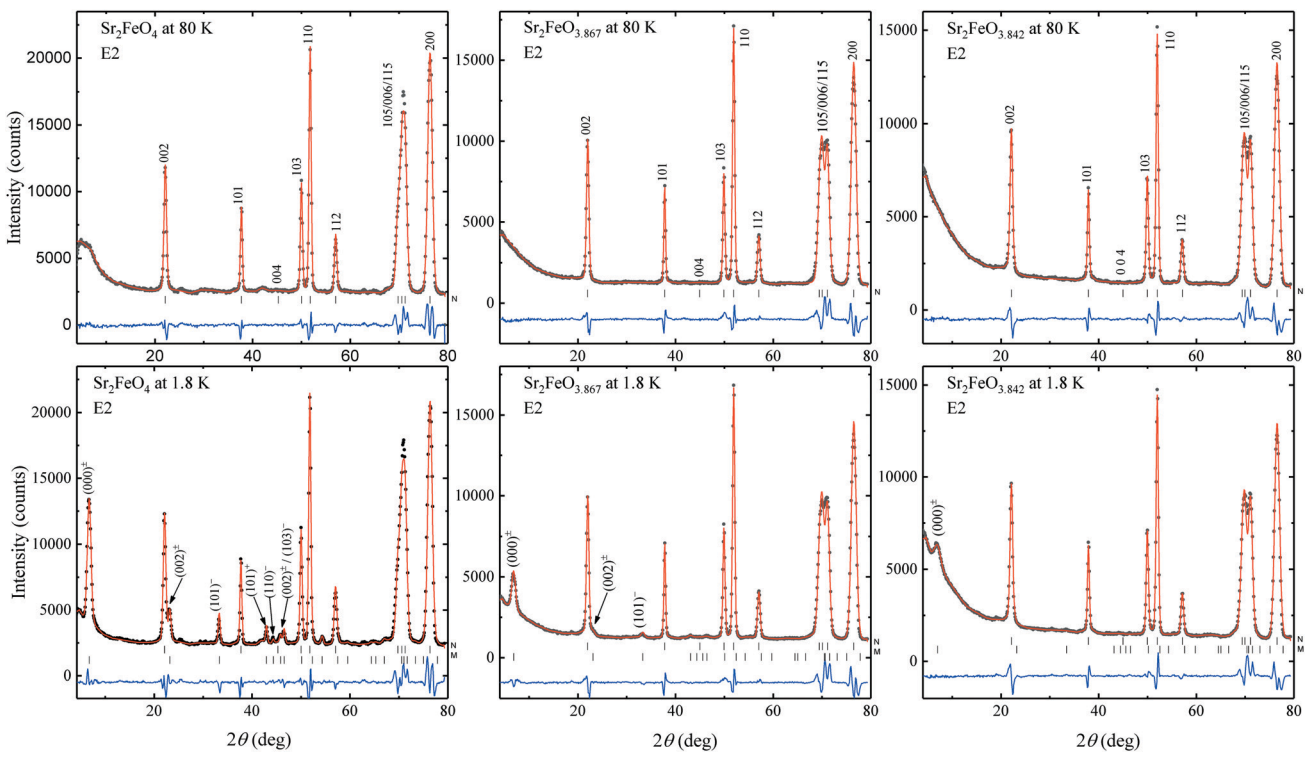

Fig. 10 Powder neutron diffraction patterns of Sr_2FeO_4, $Sr_2FeO_{3.867}$ and $Sr_2FeO_{3.842}$, collected on the instrument E2 at 1.8 and 80 K. The observed magnetic reflections at 1.8 K are generated with the rule $(hkl)_M = (hkl)_N \pm \boldsymbol{k}$, where the incommensurate propagation vector is found to be $\boldsymbol{k} = (\tau, \tau, 0)$ with $\tau = 0.137(1)$. The calculated patterns (red solid lines) are compared with the observations (black-filled circles). The positions of the nuclear (N) and generated magnetic (M) reflections (black bars) as well as the difference patterns ($I_{obs} - I_{cal}$) (blue solid lines) are also shown.

Table 1 Results of the Rietveld refinements of the powder neutron diffraction data of Sr_2FeO_{4-x} collected at 1.8 and 80 K. The residuals of the crystal and magnetic structure refinements are defined as $R_F = (\sum||F_{obs}| - |F_{calc}||/\sum|F_{obs}|)$ and $R_M = (\sum||I_{obs}| - |I_{calc}||/\sum|I_{obs}|)$, respectively. The crystal structure was refined in the tetragonal space group *I*4/*mmm*, where the Sr and O1 atoms are located at the Wyckoff position 4e(0,0,*z*), and the Fe and O2 atoms at the positions 2a(0,0,0) and 4c(0,$\frac{1}{2}$,0), respectively. Sr_2FeO_4 adopts an elliptical cycloidal spin structure and the two O deficient samples a circular helix. Using Model II of ref. 39 the spin ellipse turns slightly out of the *ab* plane around the axis along [1$\bar{1}$0]. Listed are the minor and major moments μ_{min} and μ_{max}, the averaged moment μ_{av}, the tilting angle β of the ellipse or circle to the *c* axis and the component τ of the propagation vector $\boldsymbol{k} = (\tau, \tau, 0)$. Also shown are the estimated correlation lengths ξ, the measured and calculated half widths at half maximum (HWHM) of the satellite $(000)^{\pm}$ labeled as $\Delta\theta_{obs}$ and $\Delta\theta_{sam}$, respectively

Sample	Sr_2FeO_4		$Sr_2FeO_{3.867}$		$Sr_2FeO_{3.847}$	
T [K]	1.8	80	1.8	80	1.8	80
a [Å]	3.8459(3)	3.8457(4)	3.8409(3)	3.8414(4)	3.8473(3)	3.8480(4)
c [Å]	12.374(2)	12.370(2)	12.431(2)	12.432(3)	12.475(2)	12.474(2)
V [Å^3]	183.97(6)	183.89(7)	183.38(6)	183.47(8)	184.64(6)	184.71(7)
z(Sr)	0.3567(3)	0.3554(3)	0.3564(3)	0.3566(4)	0.3578(3)	0.3576(4)
z(O1)	0.1589(4)	0.1596(4)	0.1567(4)	0.1569(5)	0.1551(3)	0.1553(4)
d_{ap}(Fe–O1) [Å]	1.967(5)	1.975(6)	1.947(5)	1.948(6)	1.934(5)	1.937(6)
d_{eq}(Fe–O2) [Å]	1.9279(2)	1.9278(2)	1.9204(2)	1.9208(2)	1.9236(2)	1.9240(2)
R_F	0.021	0.027	0.021	0.025	0.018	0.024
μ_{min}(Fe) [μ_B]	2.1(2)/1.9(2)[a]	—	1.27(17)	—	1.23(5)	—
μ_{max}(Fe) [μ_B]	3.31(8)/3.46(5)[a]	—	1.46(15)	—	1.23	—
μ_{av}(Fe) [μ_B]	2.65(6)	—	1.33(3)	—	1.23(5)	—
β (°)	−65(7)/−63(16)[a]	—	0	—	0	—
τ	0.13696(14)	—	0.1372(4)	—	0.1371(10)	—
R_M	0.030	—	0.069	—	0.131	—
$\Delta\theta_{obs}$ [°]	0.446	—	0.475	—	0.731	—
$\Delta\theta_{sam}$ [°]	0	—	0.162	—	0.579	—
ξ [Å]	—	—	67	—	19	—

[a] From ref. 39, where the magnetic structure was analyzed based on the intensities of magnetic Bragg reflections, while here we performed Rietveld refinements using model II of ref. 39.

investigate in detail the magnetic structures since all magnetic reflections appear in the measured 2θ range. It is apparent from Fig. 10 that the strongest magnetic satellites [indexed as $(000)^{\pm}$ or $(\tau, \tau, 0)$] of stoichiometric Sr_2FeO_4 and the two oxygen-deficient compounds appear practically at the same scattering angle of $2\theta = 6.9°$. Thus, the spin structures of the three compounds can be described by a propagation vector $\boldsymbol{k} = (\tau, \tau, 0)$ with $\tau = 0.137$. Recently, we have shown that stoichiometric Sr_2FeO_4 adopts a cycloidal elliptical spin spiral with a pronounced modulation of the magnetic moments between $\mu_{min} = 1.9\ \mu_B$ and $\mu_{max} = 3.5\ \mu_B$, although a certain out-of-plane tilting of the ellipse of about 27° (or a tilting angle to the *c* axis of about 63°) cannot be excluded.[39] According to Model II of ref. 39 the ellipse turns around the axis [1$\bar{1}$0] which keeps μ_{max} parallel to this axis. Thus, the component μ_{min} may partially turn out of the *ab* plane in the direction to the *c* axis.

Rietveld refinement of the pattern of $Sr_2FeO_{3.87}$ at 1.8 K resulted in comparable moment components $\mu_{min} = 1.27(17)\ \mu_B$ and $\mu_{max} = 1.46(15)\ \mu_B$ which suggests that the anisotropy in the moments is much reduced compared to Sr_2FeO_4. The averaged magnetic moment $\mu_{av} = 1.33(3)\ \mu_B$ is reduced by a factor of 2 compared to $\mu_{av} = 2.65(6)\ \mu_B$ of the parent compound. The refinement of the tilting angle to the *c* axis leads to a value of 20(15)° which is not significantly different from zero, suggesting that one of the magnetic components is probably oriented parallel to the *c* axis. Thus, in the final refinement we assumed the presence of a circular helix, where the two components of the moment are aligned now parallel to the directions [1$\bar{1}$0] and [001]. A somewhat increased oxygen deficiency in $Sr_2FeO_{3.84}$ leads to further reduction of the magnetic moment reaching the smaller value $\mu_{av} = 1.23(5)\ \mu_B$. The results of the refinements are summarized in Table 1.

In Fig. 11(a–c) the thermal variation of the averaged magnetic moments μ_{av}, the component τ of the propagation vector $\boldsymbol{k} = (\tau, \tau, 0)$, as well as the shapes of the magnetic $(000)^{\pm}$ peaks are shown. Most remarkably, only the magnetic moments and peak shapes are strongly changed in the oxygen-deficient samples, whereas the vector component τ and the Néel temperature T_N remain nearly the same as for Sr_2FeO_4. The vector component τ slightly decreases with increasing temperature for each sample as well as with increasing O deficiency. Our results suggest that oxygen deficiency mainly changes the shape and orientation of the spiral spin configuration while the propagation vector and therefore the rotation angle between adjacent spins remains the same. The spin structures of stoichiometric Sr_2FeO_4 and $Sr_2FeO_{3.87}$ are illustrated in Fig. 12.

To compare directly the magnetic intensity and peak shapes of the satellites $(000)^{\pm}$ the overall scale factors are normalized for all three samples in Fig. 11(c). To analyze the degree of peak broadening of the O-deficient samples more quantitatively we used the profile function parameters determined for the stoichiometric Sr_2FeO_4 sample. For Sr_2FeO_4 we assumed a perfect long-range magnetic order. Thus, its half width at half maximum HWHM (HWHM = FWHM/2, where FWHM is the full width at half maximum) represents the instrumental resolution (labeled as $\Delta\theta_{instr}$). While the difference between the moments of the two O-deficient samples is small, the peak width is strongly increased for $Sr_2FeO_{3.84}$ as shown in the insert of

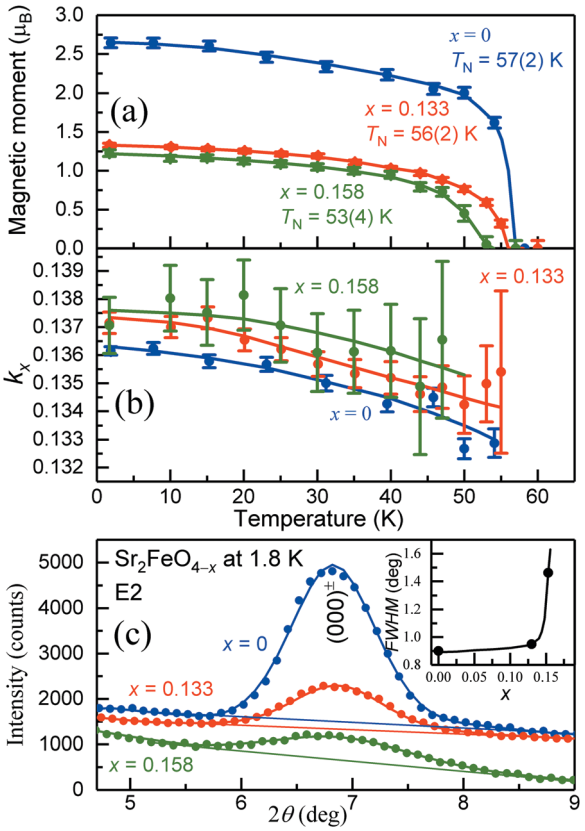

Fig. 11 Results of the neutron diffraction study of samples of Sr_2FeO_{4-x} with x = 0, 0.133 and 0.158. (a and b) Temperature dependence of the total magnetic moments and vector components k_x of Sr_2FeO_{4-x}. The averaged moments of Sr_2FeO_4 were determined from the components μ_{min} and μ_{max} of the ellipse taken from ref. 39. For the two oxygen-deficient samples the magnitudes of μ_{min} and μ_{max} were found to be similar indicating the presence of circular spiral. The solid lines are guides for the eye. (c) Change of the peak shape and intensity of the strongest magnetic satellite $(000)^{\pm}$ at 1.8 K with increasing oxygen deficiency. The insert shows the variation of the observed full widths at half maximum (FWHM).

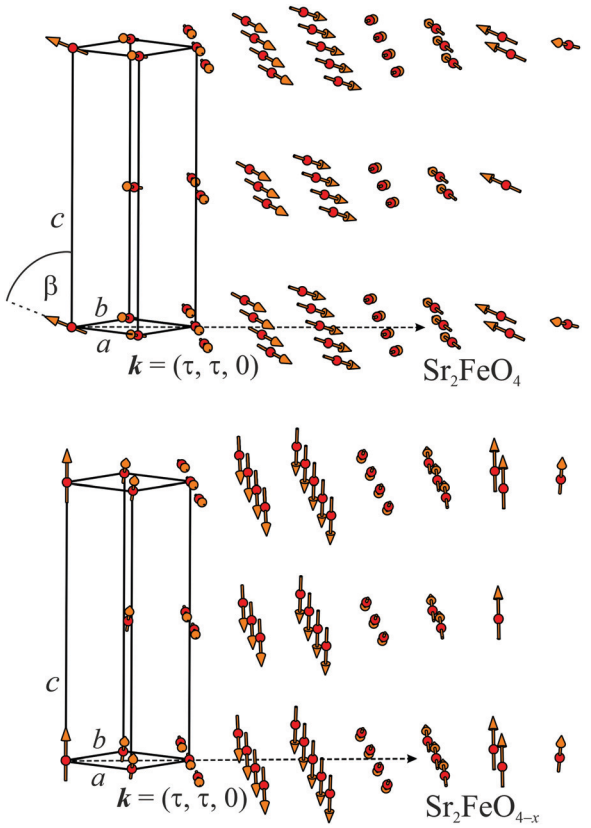

Fig. 12 Incommensurate magnetic ordering in Sr_2FeO_{4-x} with the propagation vector $\boldsymbol{k}$ = (τ, τ, 0). The magnetic moments of the Fe atoms form ferromagnetic layers perpendicular to the propagation vector $\boldsymbol{k}$ pointing along the [110] direction. Stoichiometric Sr_2FeO_4 adopts a cycloidal elliptical spin spiral, where the magnetic moments are aligned within the tetragonal *ab* plane. Nevertheless, a small out-of-plane tilting of the ellipse cannot be excluded, where the moments are tilted away from the *c* axis by an angle $\beta \sim 70°$.[39] The magnetic ordering of the oxygen-deficient compound shows the same $\boldsymbol{k}$ vector, but the tilting angle is decreased to 0° which changes the spin structure to an almost circular spiral.

Fig. 11(c). For the estimation of the magnetic correlation lengths, defined as $\xi = 1/q$, the q-values (in units of $Å^{-1}$) are determined using $q = 4\pi/\lambda \times \sin(\Delta\theta_{sam})$. The intrinsic HWHMs of Sr_2FeO_{4-x} (labeled as $\Delta\theta_{sam}$) are calculated according to $\Delta\theta_{sam} = \sqrt{(\Delta\theta_{obs}{}^2 - \Delta\theta_{instr}{}^2)}$, where $\Delta\theta_{obs}$ is the observed HWHM of the satellite $(000)^{\pm}$. The estimated correlation lengths of $Sr_2FeO_{3.87}$ and $Sr_2FeO_{3.84}$ are ξ = 67 Å and 19 Å, respectively. Further details are given in Table 1. The data suggest that increasing oxygen deficiency successively changes the spin arrangement from long-range order to a glassy state.

Such a scenario is supported by the Mössbauer spectra. The spectrum of $Sr_2FeO_{3.87}$ at 5 K indicates complete magnetic ordering or freezing of all iron moments (Fig. 9(b)). In particular, there is no drastic reduction in magnetic hyperfine fields which would be expected for a drastic reduction of the magnetic moments in the oxygen-deficient samples as suggested by the PND results. On the other hand, neutron diffraction yields average magnetic moments and only magnetically ordered regions with sufficiently large correlation length give rise to magnetic Bragg reflections. Thus, only larger-sized magnetically ordered regions are monitored in the PND experiment, whereas also the moments of smaller clusters not contributing to the neutron pattern are completely frozen at the lowest temperatures and seen by the local Mössbauer probe. This explains why the apparent magnetic moments of the iron ions appear to be reduced although Mössbauer spectra still reveal large hyperfine fields. A comparison of the magnetic moments of $Sr_2FeO_{3.87}$ and Sr_2FeO_4 suggests that only about 50% of the sample volume in the former shows long-range magnetic order detectable in PND experiments. This compares well with the area fraction of about 45% magnetically ordered phase in the 30 K Mössbauer spectrum of $Sr_2FeO_{3.87}$, whereas the other part is already paramagnetic. This fraction can be assigned to smaller magnetic clusters which do not contribute to magnetic Bragg reflections in the PND pattern. In $Sr_2FeO_{3.84}$ the coherence length is reduced and in fact the Mössbauer spectra of a sample at 30 K (Fig. S4, ESI†) show a decreased fraction of

magnetically ordered sites which suggests a larger fraction of small magnetic clusters.

It is reasonable to attribute the long-range ordered magnetic regions detectable by powder neutron diffraction to regions where the exchange network is intact enough to maintain a spiral spin structure while the smaller clusters correspond to more disturbed regions. The varying magnetic properties may be related to some inhomogeneity in oxygen deficiency x but it is not clear whether there is a real phase separation which would imply vacancy clustering or ordering. It is known that the magnetic properties of perovskites featuring partial cation order at the transition metal site indeed depend much on the local composition and structure which is not readily apparent from diffraction studies but requires additional microstructural investigations.[57] Our Mössbauer studies described above and the spectra depicted in Fig. S5 (ESI†) indicate possible variations in the microstructure in Sr_2FeO_{4-x} materials from different synthesis runs.

4. Conclusions

In this work we have explored the K_2NiF_4-type oxygen-deficient system Sr_2FeO_{4-x} by heating stoichiometric Sr_2FeO_4 in well-defined oxygen partial pressures which were controlled by solid state electrolyte coulometry. Heating to temperatures up to 550 °C allows to prepare samples with x up to about 0.2, while annealing at higher temperatures leads to decomposition into SrO and $Sr_3Fe_2O_{7-x}$. The change of lattice parameters with increasing x suggests that oxygen atoms are mainly removed from the FeO_2 planes, which has drastic consequences for the magnetic properties. Our magnetization, Mössbauer, and powder neutron diffraction studies on Sr_2FeO_{4-x} samples with x = 0.13 and x = 0.16 suggest fragmentation of the magnetic exchange network owing to the oxygen defects and the creation of Fe^{3+} sites. This leads to the coexistence of larger domains which are long-range ordered and possibly adopt a circular helical spin structure and smaller magnetic clusters with reduced ordering or freezing temperatures. Further studies on Sr_2FeO_{4-x} and related cation substituted phases including transport measurements may be of interest with respect to a potential relevance of the system for applications as mixed anionic conductors below 700 °C and in catalysis.

Conflicts of interest

There are no conflicts to declare.

Acknowledgements

We are grateful to Ralf Koban for help with magnetization measurements and Marcus Schmidt and Susann Scharsach for performing the TGA measurement.

Open Access funding provided by the Max Planck Society.

Notes and references

1 T. Mizokawa, H. Namatame, A. Fujimori, K. Akeyama, H. Kondoh, H. Kuroda and N. Kosugi, Origin of the band gap in the negative charge-transfer-energy compound $NaCuO_2$, *Phys. Rev. Lett.*, 1991, **67**, 1638.

2 T. Mizokawa, D. I. Khomskii and G. A. Sawatzky, Spin and charge ordering in self-doped Mott insulators, *Phys. Rev. Lett.*, 2000, **61**, 11263.

3 S. Johnston, A. Mukherjee, I. Elfimov, M. Berciu and G. A. Sawatzky, Charge disproportionation without charge transfer in the rare-earth-element nickelates as a possible mechanism for the metal–insulator transition, *Phys. Rev. Lett.*, 2014, **112**, 106404.

4 R. J. Green, M. W. Haverkort and G. A. Sawatzky, Bond disproportionation and dynamical charge fluctuations in the perovskite rare-earth nickelates, *Phys. Rev. B*, 2016, **94**, 195127.

5 A. E. Bocquet, A. Fujimori, T. Mizokawa, T. Saitoh, H. Namatame, S. Suga, N. Kimizuka, Y. Takeda and M. Takano, Electronic structure of $SrFe^{4+}O_3$ and related Fe perovskites, *Phys. Rev. B: Condens. Matter Mater. Phys.*, 1992, **45**, 1561.

6 J. B. MacChesney, R. C. Sherwood and J. F. Potter, Electrical and magnetic properties of the strontium ferrates, *J. Chem. Phys.*, 1965, **43**, 1907.

7 M. Takano, N. Nakanishi, Y. Takeda, S. Naka and T. Takada, Charge disproportionation in $CaFeO_3$ studied with the Mössbauer effect, *Mater. Res. Bull.*, 1977, **12**, 923.

8 P. M. Woodward, D. E. Cox, E. Moshopoulou, A. W. Sleight and S. Morimoto, Structural studies of charge disproportionation and magnetic order in $CaFeO_3$, *Phys. Rev. B: Condens. Matter Mater. Phys.*, 2000, **62**, 844.

9 S. E. Dann, M. T. Weller, D. B. Currie, M. F. Thomas and A. D. Al-Rawwas, Structure and magnetic properties of Sr_2FeO_4 and $Sr_3Fe_2O_7$ studied by powder neutron diffraction and Mössbauer spectroscopy, *J. Mater. Chem.*, 1993, **3**, 1231.

10 P. Adler, Electronic state, magnetism, and electrical transport behavior of $Sr_3A_xFe_2O_7$ ($x \leq 0.4$, A = Ba, La), *J. Solid State Chem.*, 1997, **130**, 129.

11 K. Kuzushita, S. Morimoto, S. Nasu and S. Nakamura, Charge disproportionation and antiferromagnetic order of $Sr_3Fe_2O_7$, *J. Phys. Soc. Jpn.*, 2000, **69**, 2767.

12 J.-H. Kim, D. C. Peets, M. Reehuis, P. Adler, A. Maljuk, T. Ritschel, M. C. Allison, J. Geck, J. R. L. Mardegan, P. J. Bereciartua Perez, S. Francoual, A. C. Walters, T. Keller, P. M. Abdala, P. Pattison, P. Dosanjh and B. Keimer, Hidden charge order in an iron oxide square-lattice compound, *Phys. Rev. Lett.*, 2021, **127**, 097203.

13 I. Yamada, K. Takata, N. Hayashi, S. Shimokura, M. Azuma, S. Mori, S. Muramaka, Y. Shimakawa and M. Takano, A perovskite containing quadrivalent iron as a charge-disproportionated ferrimagnet, *Angew. Chem., Int. Ed.*, 2008, **47**, 7032.

14 Y. Hosaka, N. Ichikawa, T. Saitoh, P. Manuel, D. Khalyavin, J. P. Attfield and Y. Shimakawa, Two-dimensional charge

disproportionation of the unusual valence state Fe^{4+} in a layered double perovskite, *J. Am. Chem. Soc.*, 2015, **137**, 7468.

15 M. Takano, S. Nasu, T. Abe, K. Yamamoto, S. Endo, Y. Takeda and J. B. Goodenough, Pressure-induced high-spin to low-spin transition in $CaFeO_3$, *Phys. Rev. Lett.*, 1991, **67**, 3267.

16 P. Adler, U. Schwarz, K. Syassen, G. K. Rozenberg, G. Yu. Machiavariani, A. P. Milner, M. P. Pasternak and M. Hanfland, Collapse of the charge disproportionation and covalency-driven insulator-metal transition in $Sr_3Fe_2O_7$ under pressure, *Phys. Rev. B: Condens. Matter Mater. Phys.*, 1999, **60**, 4609.

17 T. Kawakami, Y. Sekiya, A. Mimura, K. Kobayashi, K. Tokumichi, I. Yamada, M. Mizukami, N. Kawamura, Y. Shimakawa, Y. Ohishi, N. Hirao, N. Ishimatsu, N. Hayashi and M. Takano, Two-step suppression of charge disproportionation in $CaCu_3Fe_4O_{12}$ under pressure, *J. Phys. Soc. Jpn.*, 2016, **85**, 034716.

18 T. Takeda, Y. Yamaguchi and H. Watanabe, Magnetic structure of $SrFeO_3$, *J. Phys. Soc. Jpn.*, 1972, **33**, 967.

19 N. Hayashi, T. Yamamoto, H. Kageyama, M. Nishi, Y. Watanabe, T. Kawakami, Y. Matsushita, A. Fujimori and M. Takano, $BaFeO_3$: a ferromagnetic iron oxide, *Angew. Chem., Int. Ed.*, 2011, **50**, 12547.

20 J.-H. Kim, A. Jain, M. Reehuis, D. C. Peets, C. Ulrich, J. T. Park, E. Faulhaber, A. Hoser, H. C. Walker, D. T. Adroja, A. C. Walters, D. S. Inosov, A. Maljuk and B. Keimer, Competing exchange interactions at the verge of a metal-insulator transition in the two-dimensional spiral magnet $Sr_3Fe_2O_7$, *Phys. Rev. Lett.*, 2014, **113**, 147206.

21 S. Ishiwata, M. Tokunaga, Y. Kaneko, D. Okuyama, S. Wakimoto, K. Kakurai, T. Arima, Y. Taguchi and Y. Tokura, Versatile helimagnetic phases under magnetic fields in cubic perovskite $SrFeO_3$, *Phys. Rev. B: Condens. Matter Mater. Phys.*, 2011, **84**, 05447.

22 S. Chakraverty, T. Matsuda, H. Wadati, J. Okamoto, Y. Yamasaki, H. Nakao, Y. Murakami, S. Ishiwata, M. Kawasaki, Y. Taguchi, Y. Tokura and H. Y. Hwang, Multiple helimagnetic phases and topological Hall effect in epitaxial thin films of pristine and Co-doped $SrFeO_3$, *Phys. Rev. B: Condens. Matter Mater. Phys.*, 2013, **88**, 220405(R).

23 S. Ishiwata, T. Nakajima, J. H. Kim, D. S. Inosov, N. Kanazawa, J. S. White, J. L. Gavilano, R. Geogii, K. Seemann, G. Brandl, P. Manuel, D. D. Khalyavin, S. Seki, Y. Tokunaga, M. Kinoshita, Y. W. Long, Y. Kaneko, Y. Taguchi, T. Arima, B. Keimer and Y. Tokura, Emergent topological spin structures in the centrosymmetric cubic perovskite $SrFeO_3$, *Phys. Rev. B: Condens. Matter Mater. Phys.*, 2020, **101**, 134406.

24 J. P. Hodges, S. Short, J. D. Jorgensen, X. Xiong, B. Dabrowski, S. M. Mini and C. W. Kimball, Evolution of the oxygen-vacancy ordered crystal structures in the perovskite series $Sr_nFe_nO_{3n+1}$ (n = 2, 4, 8, and ∞), and the relationship to electronic and magnetic properties, *J. Solid State Chem.*, 2006, **151**, 190.

25 M. Reehuis, C. Ulrich, A. Maljuk, Ch Niedermeyer, B. Ouladdiaf, A. Hoser, T. Hofmann and B. Keimer, Neutron diffraction study of spin and charge ordering in $SrFeO_{3-\delta}$, *Phys. Rev. B: Condens. Matter Mater. Phys.*, 2012, **85**, 184109.

26 A. Lebon, P. Adler, C. Bernhard, A. V. Boris, A. V. Pimenov, A. Maljuk, C. T. Lin, C. Ulrich and B. Keimer, Magnetism, charge order, and giant magnetoresistance in $SrFeO_{3-\delta}$ single crystals, *Phys. Rev. Lett.*, 2004, **92**, 037202.

27 P. Adler, A. Lebon, V. Damljanović, C. Ulrich, C. Bernhard, A. V. Boris, A. Maljuk, C. T. Lin and B. Keimer, Magnetoresistance effects in $SrFeO_{3-\delta}$: dependence on phase composition and relation to magnetic and charge order, *Phys. Rev. B: Condens. Matter Mater. Phys.*, 2006, **73**, 094451.

28 Y. Tsujimoto, C. Tassel, N. Hayashi, T. Watanabe, H. Kageyama, K. Yoshimura, M. Takano, M. Ceretti, C. Ritter and W. Paulus, Infinite-layer iron oxide with a square-planar coordination, *Nature*, 2007, **450**, 1062.

29 D. C. Peets, J.-H. Kim, P. Dosanjh, M. Reehuis, A. Maljuk, N. Aliouone, C. Ulrich and B. Keimer, Magnetic phase diagram of $Sr_3Fe_2O_{7-\delta}$, *Phys. Rev. B: Condens. Matter Mater. Phys.*, 2013, **87**, 214410.

30 P. K. Gallagher, J. B. MacChesney and D. N. E. Buchanan, Mössbauer effect in the system $Sr_3Fe_2O_{6-7}$, *J. Chem. Phys.*, 1966, **45**, 2466.

31 S. E. Dann, M. T. Weller and D. B. Currie, Structure and oxygen stoichiometry in $Sr_3Fe_2O_{7-y}$, $0 \leq y \leq 1.0$, *J. Solid State Chem.*, 1992, **97**, 179.

32 H. Kageyama, T. Watanabe, Y. Tsujimoto, A. Kitada, Y. Samida, K. Kanamori, K. Yoshimura, N. Hayashi, S. Muranaka, M. Takano, M. Ceretti, W. Paulus, C. Ritter and G. André, Spin-ladder iron oxide: $Sr_3Fe_2O_5$, *Angew. Chem., Int. Ed.*, 2008, **47**, 5740.

33 B. Li, S. He, J. Li, X. Yue, J. T. S. Irvine, D. Xie, J. Ni and C. Ni, A Ce/Ru codoped $SrFeO_{3-\delta}$ perovskite for a coke-resistant anode of a symmetrical solid oxide fuel cell, *ACS Catal.*, 2020, **10**, 14398.

34 K. Wiik, S. Aasland, H. L. Hansen, I. L. Tangen and R. Ødegård, Oxygen permeation in the system $SrFeO_{3-x}$–$SrCoO_{3-y}$, *Solid State Ionics*, 2002, **152–153**, 675.

35 K. Tamai, S. Hosokawa, K. Kato, H. Asakura, K. Teramura and T. Tanaka, Low-temperaure NO oxidation using lattice oxygen in Fe-site substituted $SrFeO_{3-\delta}$, *Phys. Chem. Chem. Phys.*, 2020, **22**, 24181.

36 R. Scholder, H. v Bunsen and W. Zeiss, Über Orthoferrate, *Z. Anorg. Allg. Chem.*, 1956, **283**, 330.

37 P. Adler, Properties of K_2NiF_4-type oxides $Sr_2FeO_{\sim 4}$, *J. Solid State Chem.*, 1994, **108**, 275.

38 P. Adler, A. F. Goncharov, K. Syassen and E. Schönherr, Optical reflectivity and Raman spectra of Sr_2FeO_4 under pressure, *Phys. Rev. B: Condens. Matter Mater. Phys.*, 1994, **50**, 11396.

39 P. Adler, M. Reehuis, N. Stüßer, S. A. Medvedev, M. Nicklas, D. C. Peets, J. Bertinshaw, C. K. Christensen, M. Etter, A. Hoser, L. Schröder, P. Merz, W. Schnelle, A. Schulz, Q. Mu, D. Bessas, A. Chumakov, M. Jansen and C. Felser, Spiral magnetism, spin flop, and pressure-induced

ferromagnetism in the negative charge-transfer-gap insulator Sr_2FeO_4, *Phys. Rev. B: Condens. Matter Mater. Phys.*, 2022, **105**, 054417.

40 G. K. Rozenberg, A. P. Milner, M. P. Pasternak, G. R. Hearne and R. D. Taylor, Experimental confirmation of a p–p intraband gap in Sr_2FeO_4, *Phys. Rev. B: Condens. Matter Mater. Phys.*, 1998, **58**, 10283.

41 Y. Takeda, K. Imayoshi, N. Imanishi, O. Yamamoto and M. Takano, Preparation and characterization of $Sr_{2-x}La_xFeO_4$ ($0 \leq x \leq 1$), *J. Mater. Chem.*, 1994, **4**, 19.

42 T. Omata, K. Ueda, H. Hosono, M. Katada, N. Ueda and H. Kawazoe, Electrical and magnetic properties of hole-doped $Sr_{1+x}La_{1-x}FeO_4$, *Phys. Rev. B: Condens. Matter Mater. Phys.*, 1994, **49**, 10194.

43 Q. Zhao, M. D. Smith and H.-C. zur Loye, Crystal growth and structure determination of the mixed-valent iron(III/IV) oxides $Sr_{2-x}Ln_xFeO_4$ (Ln = Nd, Sm, Eu), *J. Chem. Crystallogr.*, 2011, **41**, 674.

44 C. Tassel, L. Seinberg, N. Hayashi, S. Ganesanpotti, Y. Ajiro, Y. Kobayashi and H. Kageyama, Sr_2FeO_3 with stacked infinite chains of FeO_4 square planes, *Inorg. Chem.*, 2013, **52**, 6096.

45 C. Linke and M. Jansen, Über Ag_2SnO_3, das erste Silberstannat, *Z. Anorg. Allg. Chem.*, 1997, **623**, 1441.

46 H. M. Rietveld, A profile refinement method for nuclear and magnetic structures, *J. Appl. Crystallogr.*, 1969, **2**, 65.

47 L. Akselrud and Y. Grin, WinCSD: software package for crystallographic calculations (Version 4), *J. Appl. Crystallogr.*, 2014, **47**, 803.

48 Z. Klencsár, E. Kuzmann and A. Vértes, User-friendly software for Mössbauer spectrum analysis, *J. Radioanal. Nucl. Chem.*, 1996, **210**, 105.

49 J. Rodríguez-Carvajal, Recent advances in magnetic structure determination by neutron powder diffraction, *Phys. B*, 1993, **192**, 55.

50 V. F. Sears, in *International Tables for Crystallography*, ed. A. J. C. Wilson, Kluwer Academic Publishers, Dordrecht/Boston/London, 1995, vol. C, p. 383.

51 P. J. Brown, in *International Tables for Crystallography*, ed. A. J. C. Wilson, Kluwer Academic Publishers, Dordrecht/Boston/London, 1995, vol. C, p. 391.

52 K. Teske, H. Oppermann and G. Stöver, Zur Bestimmung der Phasenbreite von Zinkoxid, *Z. Anorg. Allg. Chem.*, 1984, **511**, 72.

53 M. Bode, K. Teske and H. Ullmann, Fest-Elektrolyt-Coulometrie (FEC). Eine vielseitige Methode zur Untersuchung von Gas-Festkörper-Wechselwirkungen, *GIT-Fachz. Lab*, 1994, **38**, 495.

54 K. Teske, H. Ullmann and N. Trofimenko, Thermal analysis of transition metal and rare earth oxide system-gas interactions by a solid electrolyte-based coulometric technique, *J. Thermal Anal.*, 1997, **49**, 1211.

55 V. Vashook, J. Zosel and U. Guth, Oxygen solid electrolyte coulometry (SEC), *J. Solid State Electrochem.*, 2012, **16**, 3401.

56 S. E. Dann, M. T. Weller and D. B. Currie, Synthesis and structure of Sr_2FeO_4, *J. Solid State Chem.*, 1991, **92**, 237.

57 M. Hendrickx, Y. Tang, E. C. Hunter, P. D. Battle and J. Hadermann, Structural and magnetic properties of the perovskites $A_2LaFe_2SbO_9$ (A = Ca, Sr, Ba), *J. Solid State Chem.*, 2021, **295**, 121914.